

Visually Assisted Anti-lock Braking System

Michal Bahník, Dominik Filyo, David Pekarek, Martin Vlasimský, Jan Cech, Tomas Hanis, Martin Hromčík
Faculty of Electrical Engineering, Czech Technical University in Prague

Abstract—The concept of a visually-assisted anti-lock braking system (ABS) is presented. The road conditions in front of the vehicle are assessed in real time based on camera data. The surface type classification (tarmac, gravel, ice, etc.) and related road friction properties are provided to the braking control algorithm in order to adjust the vehicle response accordingly. The system was implemented and tested in simulations as well as on an instrumented sub-scale vehicle. Simulations and experimental results quantitatively demonstrate the benefits of the proposed system in critical maneuvers, such as emergency braking and collision avoidance.

I. INTRODUCTION

Vehicle stabilization and control solutions which could benefit from friction and adhesion recognition systems are crucial from the ride safety perspective. Anti-lock braking systems (ABS) and Electronic Stabilization Programs (ESP) are mandatory and requested by law in current cars. These systems rely at present on pure feedback schemes. Corrective actions are executed as a response to measured motions of the vehicle, and the road conditions are only implicitly estimated from events like a locked wheel or slippage of the car. Namely the ABS system response is based on the vehicle reactions to excessive braking input solely, and no a-priori information on the road conditions is employed. On the contrary, experienced human drivers take into account if the road in front of the car is (or seems to be) wet or icy and adjust their actions accordingly.

Our idea is to implement this functionality. The system has the potential to significantly increase safety in critical accident-threatening situations. To the best of our knowledge, we are not aware of any academic or commercial system taking the friction parameters estimated by vision into account to set the parameters of a braking, traction, or stability system (ABS, ASR, ESP respectively). In current systems, the surface friction (and thus maximum braking or acceleration force) is estimated in an iterative fashion in a closed loop to prevent locking the wheels or losing the traction. This approach is both slow and sub-optimal, especially in the case of heterogeneous surfaces composed of segments with dramatically varying friction coefficients (like dry tarmac with icy, wet, or dirt patches). We propose the system that will predict friction properties of the surface from a camera before the car approaches it, and it will adjust the parameters of the vehicle controller accordingly in advance.

The rest of the paper is structured as follows: Related works are discussed in Sec. II. The method is presented in Sec. III. Simulations are described in Sec. IV. Experiments are given in Sec. V. Finally Sec. VI concludes the paper.

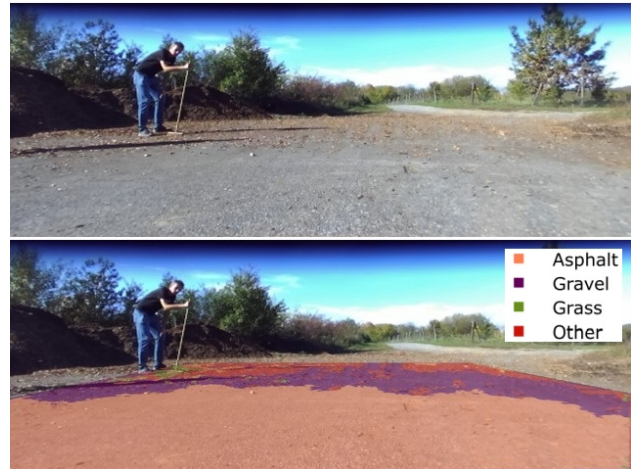


Fig. 1. We propose a system that visually recognizes the surface type ahead of the vehicle and sets the anti-lock braking algorithm to fit its friction properties. Top image is captured by a test vehicle camera showing an asphalt road covered with a layer of gravel far away. The recognition results are shown below. In our experiments we demonstrate the proposed system extends the maneuverability and shortens the stopping distance especially on uneven slippery surfaces.

II. RELATED WORK

The general idea of ADAS – the Advanced Driver Assistance Systems – augmented by sensors for environment awareness and obstacle detection has given rise to numerous successful technologies in the past decades. A recent survey on the environment perception of intelligent vehicles can be found in [1]. Adaptive cruise control and lane keeping assistants are standard nowadays, as are the automatic/assisted parking and emergency braking systems [2].

Applications of on-board cameras for assessment of road conditions, with implications towards systems of active vehicle stabilization and control, also exist, they are however much less common. On the commercial level, the Mercedes’s Magic Body Control systems for high class limousines is arguably the best known and most evolved example [3]. It utilizes stereo cameras to monitor the surface of the road in front of the car. Identified bumps and potholes are communicated in real time to the active suspension system which is programmed accordingly to compensate such disturbances when/before the chassis meets them.

Commercial camera-based solutions for estimation of the friction and adhesion properties of the road do not exist. A few research reports on the topic however appeared recently. In [4] a new methodology is presented for detection of wet areas and puddles using a stereo camera with polarization fil-

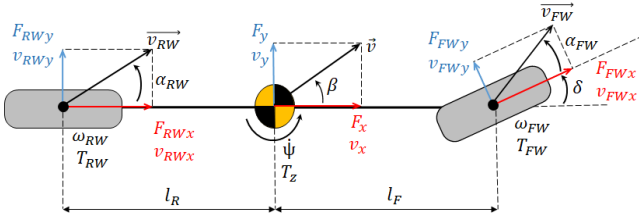


Fig. 2. Single-track model.

ters. It relies on color information for hypothesis generation, and a support vector machine for hypothesis verification. Experimental verification (with a static camera) proving good performance and robustness are presented. An automatic image recognition system for winter road surface condition classification was proposed in [5]. Selected reports on non-camera approaches follow: detection of ice formations on road surfaces using infrared thermometers is studied in [6]. Furthermore, detection of water on the road as well as ice and snow using a cost-effective infrared sensor was studied in [7]. Finally, several works were reported based on millimeter wave radar [8], [9], [10].

The distinguishing feature of our contribution with respect to existing reports is that we have really “closed the loop”:

- we implemented the surface recognition system as well as a selected vehicle control solution (namely ABS);
- both in simulations and on a sub-scale experimental vehicle;
- and we give specific and quantitative results on performance gains for this combination.

III. PROPOSED METHOD

The method proposed in this paper utilizes an image processing tool-chain for road condition classification. The anti-lock braking system then takes this information into account to improve its robustness and performance. The complete system was modelled, simulated, and experimentally verified as described in detail in the following text.

A. Mathematical models

The vehicle model: The nonlinear single-track model [11] is considered, see Fig. 2. The model state variables are $x = (|\vec{v}|, \beta, \dot{\psi}, \omega_{FW}, \omega_{RW})$, where $|\vec{v}| [m/s]$ is the vehicle velocity at the center of gravity (CG), $\beta [rad]$ is the vehicle side-slip angle at CG, $\dot{\psi} [rad/s]$ is the cornering speed at CG, and $\omega_{FW} [rad/s]$ and $\omega_{RW} [rad/s]$ are the rotational velocities of the front and rear wheels respectively. In our case the control inputs are the torques applied on the front and rear wheels respectively, $u = (T_{FW}, T_{RW})$, only the longitudinal dynamics/control shall be considered.

The dynamics of the single track model is described by the following differential equations:

$$\begin{aligned} \dot{\beta} &= -\dot{\psi} + \frac{1}{m|\vec{v}|}(\cos \beta F_y - \sin \beta F_x), \\ |\dot{\vec{v}}| &= \frac{1}{m}(\sin \beta F_y + \cos \beta F_x), \\ \ddot{\psi} &= \frac{1}{I_z} T_z, \end{aligned} \quad (1)$$

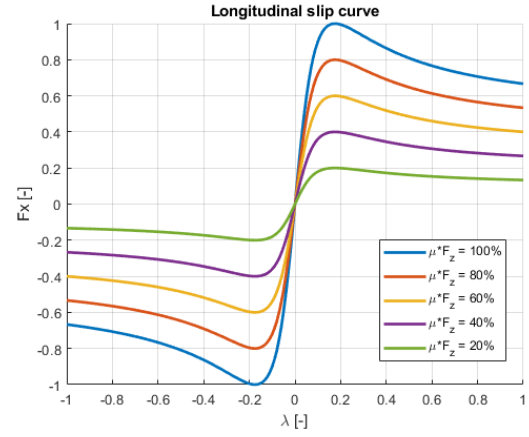


Fig. 3. Longitudinal slip curve.

where the $F_x [N]$ is the force acting in longitudinal direction at CG, $F_y [N]$ is the force acting in lateral direction at CG and $T_z [Nm]$ is the cornering torque at CG. The force vectors and the cornering torque at CG are results of the tire forces generated by each wheel:

$$\begin{aligned} F_x &= F_{FWx} \cdot \cos \delta - F_{FWy} \cdot \sin \delta + F_{RWx}, \\ F_y &= F_{FWx} \cdot \sin \delta + F_{FWy} \cdot \cos \delta + F_{RWy}, \\ T_z &= l_f \cdot F_{FWx} \cdot \sin \delta + l_f \cdot F_{FWy} \cdot \cos \delta - l_r \cdot F_{RWy}. \end{aligned} \quad (2)$$

The $F_{F/RWx}$ are longitudinal forces generated by the front/rear wheel respectively, and $F_{F/RWy}$ are related lateral forces.

The wheel longitudinal traction force is governed by the wheel slip-ratio $\lambda [-]$ defined by equation (3) for the front wheel¹,

$$\lambda_{FW} = \frac{\omega_{FW} \cdot r - |\vec{v}|}{\max(|\omega_{FW}| \cdot r, |\vec{v}|)}, \quad (3)$$

where $r[m]$ is the wheel radius.

The dependency of longitudinal forces generated by the wheels F_{FWx} and F_{RWx} on the wheel slip-ratio is represented by the slip curve. In our case the Pacejka magic formula (with its parameters B, C, D and E , see [12]) is considered, see Fig. 3. In addition, it is proportional to the wheel normal loading $F_z [N]$ and the road coefficient of friction $\mu [-]$:

$$F_{FWx}(\lambda) = D\mu F_z \sin(C \arctan(B\lambda - E(B\lambda - \arctan(B\lambda)))), \quad (4)$$

The wheel model: The front wheel equation of motion² reads

$$J_{FWy} \cdot \dot{\omega}_{FW} = T_{FW} + F_{FWx}(\lambda) \cdot r + T_{drag}, \quad (5)$$

where the $J_{FWy} [kg \cdot m^2]$ is the wheel moment of inertia along the wheel shaft axis, $T_{FW} [Nm]$ is the input drive/brake torque applied on the wheel, $F_{FWx} [N]$ is the longitudinal traction force generated by the wheel, and

¹The rear wheel case is identical.

²The rear wheel model is identical.

T_{drag} [Nm] represents all drag effects combined. Parameter r [m] is the wheel radius. Note that F_{FWx} is defined by equation (4) in the previous subsection.

The braking system model: The simplified dynamics of the braking system is considered in the form of a first order system combined with a time delay represented by transfer function:

$$G(s) = \frac{1}{\tau_b s + 1} \cdot e^{-T_b \cdot s}, \quad (6)$$

where $\tau_b = T_b = 0.1$ s. This model represents physical phenomena related to the braking system actuation (hydraulic pressure generation and propagation), the friction physics, and the wheel relaxation dynamics on one hand; and the lags associated with acquisition and signal processing of measured variables (the vehicle reference velocity and the angular velocities of the wheels) on the other hand.

B. The anti-locking braking algorithm

The used ABS procedure is presented in Algorithm 1. For sake of simplicity, absolute values of λ and braking torques are assumed as only the braking maneuver is considered. Both the conventional and camera-based versions share the same functionality. The additional information provided by image recognition is the locking brake torque value estimate, in the form of the *MaxBrakeTorque* and *BrakeTorqueInit* parameters.

The ABS works in cycles with two phases. First, the brake torque increases until the wheel is too loaded and it starts to lock (rapidly loses its angular momentum/velocity). Second, the release phase, where the brake torque is reduced and the wheel is relaxed (it regains its angular momentum). The braking torque rise is divided into two parts to reduce idle/low braking action time. The rapid phase (represented with brake torque increment by parameter r_1) until the predefined torque value is reached, in our case it is 80% of locking torque $T_{locking}$. The slow phase (represented with brake torque increment by parameter r_2) follows to increase the braking action and time spent just below locking braking torque $T_{locking}$. The maximum achieved braking torque is detected and set as new locking braking torque for the next cycle. The wheel locking action (triggering release phase) is detected based on the value of wheel slip-ratio crossing its maximal/locking value λ_{max} . The release phase is terminated once the wheel slip-ratio drops below its minimal value λ_{min} . The braking torque is reset to the value $k \cdot T_{locking}$ at the beginning of each release phase.

The values of the parameters $r_1, r_2, k, \lambda_{min}, \lambda_{max}$ used in the paper are presented in Table I. The algorithm reads the values of wheel slip ratio λ (see eq. 3), *MaxBrakeTorque* and *BrakeTorqueInit* in each cycle.

- For the standard ABS version (without a camera), both $MaxBrakeTorque = T_{max}$, $BrakeTorqueInit = 0$ are constant.
- For the camera-based ABS version, the estimated value of the locking braking torque is provided based on the classified surface, $MaxBrakeTorque = T_{cam}$,

Algorithm 1 Emergency braking with anti-lock system

```

while Car Not Stationary do
  Get  $\lambda$ , MaxBrakeTorque, BrakeTorqueInit
  if MaxBrakeTorque value is changed then
     $T_{locking} \leftarrow MaxBrakeTorque$ 
     $CurrentBrakeTorque \leftarrow BrakeTorqueInit$ 
  end if
  if  $\lambda < \lambda_{max}$  then
    if  $CurrentBrakeTorque < 0.8 \cdot T_{locking}$  then
       $CurrentBrakeTorque \leftarrow CurrentBrakeTorque + r_1$ 
    else
       $CurrentBrakeTorque \leftarrow CurrentBrakeTorque + r_2$ 
    end if
  else
     $T_{locking} \leftarrow CurrentBrakeTorque$ 
     $CurrentBrakeTorque \leftarrow k \cdot CurrentBrakeTorque$ 
    while TRUE do
      Get  $\lambda$ 
      if  $\lambda < \lambda_{min}$  then
        break
      end if
    end while
  end if
end while

```

r_1	r_2	k	λ_{min}	λ_{max}
1/10	1/100	0	0.15	0.21

TABLE I

ABS ALGORITHM PARAMETERS

$BrakeTorqueInit = T_{cam}$, where T_{cam} is updated in event-based fashion (once a new surface is detected).

The visual estimation mechanism for these parameters is described in the following subsection.

C. Visual Surface Recognition

A camera mounted on the vehicle is used to recognize the surface type. The problem is formulated as a semantic segmentation. It means that each pixel of the input image has a semantic label of the surface type. We train a convolutional neural network to do the prediction.

Images from the camera are first geometrically normalized by orthographic rectification (birds-eye view). The image of the rectangular area in front of the vehicle, 2.5 meters both left and right and 8 meters ahead, (5 × 8) meters, captured by the camera is warped by planar homography H into the rectangular image of size (416 × 608), see Fig. 4. The ortho-rectified images are then fed to the convolutional neural network (CNN).

The main reason for the rectification is that the system were not dependent on a particular viewpoint of the camera. It will not be necessary to retrain the CNN in case the camera viewpoint changes. The homography mapping for a new camera viewpoint or a different camera would be found and we could in theory combine multiple different

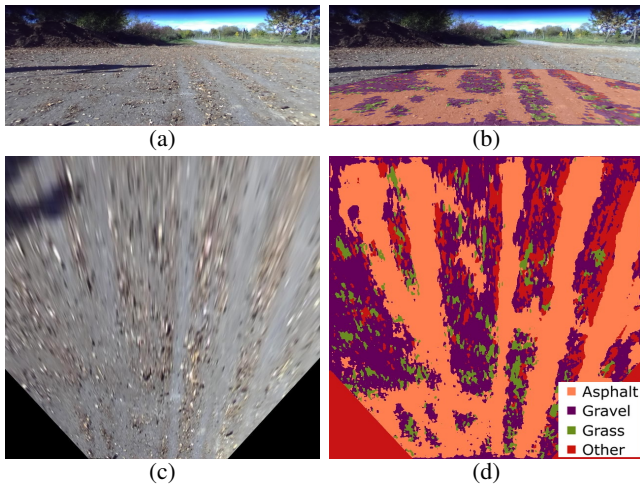


Fig. 4. Visual surface recognition. Image captured by the platform camera (a), an ortho-rectified image, i.e. ‘birds-eye’ view of the surface 5×8 meters (input of the CNN) (c), color-coded segmentation results (output of the CNN) (d), segmentation map back-projected over the input-image (b).

camera setups. Moreover, it is particularly easy to generate synthetic data and perform data augmentation when the image is orthographically rectified. We pre-train the network on large number of synthetic data with a cheap ground-truth annotation and then the network is fine-tuned on a couple of examples of real data with the manual annotation of surface types.

For demonstration and subsequent experiments we train three classes (tarmac, gravel, and grass) plus an extra class for “unknown” surface type. Each class is associated with friction properties of the surface, giving rise to input values $MaxBrakeTorque$ and $BrakeTorqueInit$ of Algorithm 1.

Synthetic image dataset was collected by stitching random patches of different surfaces, that were captured by hand-held camera (roughly ground-parallel). For the extra class, we randomly sampled patches from ImageNet dataset [13]. The images are then randomly rotated and translated. To simulate a loss of resolution at distance we warped the images by the inverse homography (to the viewpoint of our camera) and back again. Re-sampling the image does the effect of loss of detail at distance. For real data, with the manual annotation, we use a similar data augmentation, vertical flipping, in-plane rotation and a small translation.

Concerning the network architecture, we selected VGG implementation of the U-NET [14]. It is a fully convolutional neural network, an hour-glass architecture with the skip-connection. We trained on about 4k synthetic images, plus 80 real images captured by the platform camera with manual annotation. The real images have 10-times larger weight on the gradient. The training converged after 40 epochs. Quantitative results of testing are presented in Sec. V.

IV. SIMULATIONS

The emergency braking scenario was simulated and quantitatively assessed for the case of a problematic road segment. Parameters of the models (vehicle, tyres, the braking system)

were selected to represent a middle class sedan. Quantitative evaluation of the total braking distance reduction is given.

A. Scenario description

The verification scenario is designed in order to test braking capabilities of the visually-assisted ABS algorithm described in section III-B. We simulate high speed emergency braking (full brake input) to still stand, with crossing of an icy patch. The braking maneuver starts at first second of simulation with the vehicle initial speed set to 30 m/s . The vehicle starts to brake on surface with 50% of μ_{max} , representing wet tarmac. The icy patch appears in simulation time $4\text{s} - 10\text{s}$ and is simulated by drop of μ to 10% of μ_{max} . Finally the road condition is restored to 50% of μ_{max} at 10s till full stop.

B. Results

The vehicle state and control variables are presented in Fig. 5. The vehicle deceleration (Fig. 5, top plot) shows faster braking action at simulation time 1s and 10s for camera assisted ABS (blue) compared to conventional ABS (red). The overall braking distance difference can be seen from Fig. 5 bottom plot, reaching to 32.45 meters (about 14.4%) of total braking distance. The front and rear wheel variables are presented on Fig. 6 and Fig. 7 respectively.

The braking distance reduction is achieved thanks to provided information about the road, namely the locking brake torque estimate $T_{locking}$ provided to Algorithm 1. On top of that the variance of the deceleration is smaller with camera right after a surface condition change. Both effects result from a significantly reduced surface identification phase of the ABS algorithm for the camera assisted case.

The identification phase of the locking torque value $T_{locking}$ can be seen from braking torque plots (Fig. 6, Fig. 7 bottom). The camera based ABS with $T_{locking}$ set appropriately (closer to the real road conditions) has significantly shorter identification phase compared to conventional ABS with $T_{locking}$ initialized with the maximum braking torque.

The identification phase associated with ABS operation has two unfavorable impacts on braking action. First, the slower start of braking action. The camera based braking system reaches maximal deceleration in 500ms (Fig. 5 top plot; simulation time $1 - 1.5\text{s}$ and $10 - 10.5\text{s}$). The same effect can be seen from braking torque acting on wheel (Fig. 6 and Fig. 7 bottom plot; simulation time $1 - 1.5\text{s}$ and $10 - 10.5\text{s}$). The second effect is higher variance of vehicle deceleration (Fig. 5 top plot; simulation time $2 - 5\text{s}$) and maximum value of braking torque (Fig. 6 and Fig. 7 bottom plot; simulation time $1 - 5\text{s}$ and right after the surface condition change $5 - 8\text{s}$). The identification process slows convergence for standard ABS, as can be clearly seen from Fig. 6 and Fig. 7 bottom plot, simulation time $5 - 8\text{s}$ right after the surface condition change. The same tendency can be seen also for beginning of the braking maneuver, but the surface change distracts such observation.

One can argue against the unrealistic assumption of brake locking torque precise value detection. The robustness of

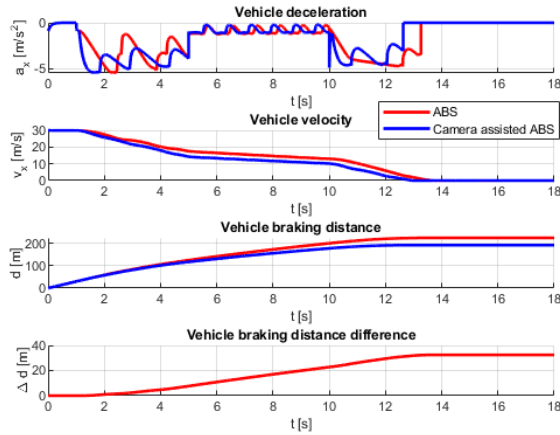


Fig. 5. The vehicle variables for braking maneuver.

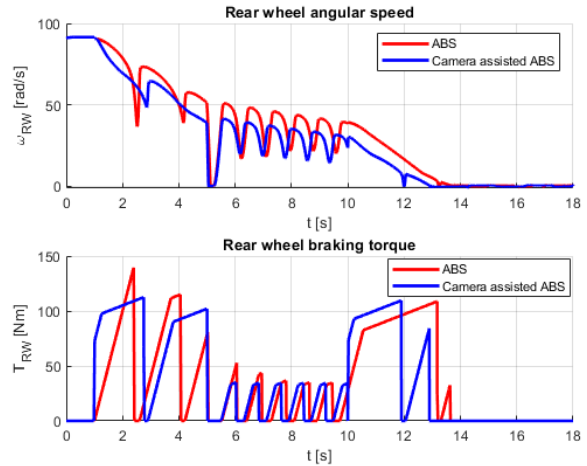


Fig. 7. The rear wheel variables for braking maneuver.

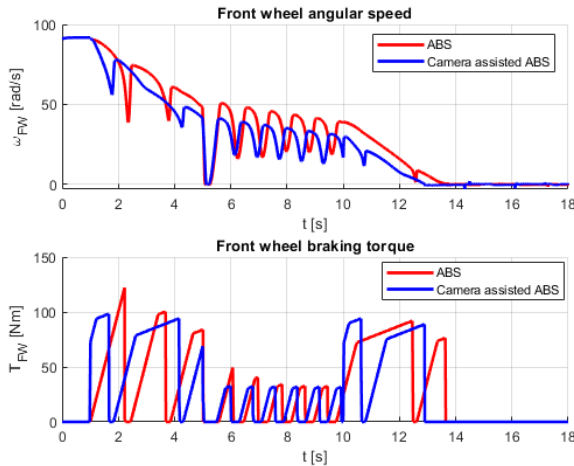


Fig. 6. The front wheel variables for braking maneuver.



Fig. 8. Experimental subscale vehicle platform.

the camera-assisted ABS with respect to this uncertainty is therefore demonstrated with the locking value of the braking torque deliberately corrupted with an error of 10% (and with the generic ABS identification process running still at the background). Even with such an imperfect a-priori information, essential reduction of the identification phase is achieved as can be seen from Fig. 6 and Fig. 7 bottom plot at time 1s and 10s.

V. EXPERIMENTS

Experiment with an instrumented subscale vehicle were conducted in order to enhance and further develop the simulation findings. Attention was paid namely to:

- Road surface classification under real conditions. The neural network trained offline was implemented on board of the car and it provides real-time classification of the surface. Reliability of the classification process by means of the confusion matrix is provided.
- Combined maneuvers/collision avoidance capability. Simultaneous intensive braking and turning scenarios were studied on gravel and tarmac. A major benefit of

ABS systems is that the steering capability of the car is preserved even at intensive braking.

- Performance gains of the camera-augmented ABS system in the combined maneuvers are quantitatively assessed.
- Robustness to surface misclassifications. We study the effects of potential surface classification errors on the overall camera-augmented ABS performance.

A. Experimental Vehicle Platform

We built a sub-scale vehicle platform around a large 1:5 RC car, equipped with a stereo-camera, IMU, GPS. Namely, we selected Losi Desert Buggy XL-E 4WD³. The model is of $0.9 \times 0.5 \times 0.3$ meters dimension, large 190 mm-diameter wheels with rubber tires, its weight (with the extra equipment) is about 15 kg. It is 4WD, electric powered BLDC motor. Top speed is reported up to 80 km/h. The RC car is very agile fitting our experiments.

We installed following sensors. ZED camera⁴, a stereo-rig, mounted onto a frame about 30 cm above the vehicle, as shown in Fig. 8. The camera has 120mm baseline, 110° field of view, $f/2.0$, 720p at 60 FPS, USB 3. We equipped the platform with the NAVIO board⁵ with IMU (accelerometer, gyro, magnetometer) and GPS. Motor RPMs were measured using Hall sensor with neodymium magnets on the main

³<http://www.losi.com/Products/Default.aspx?ProdID=LOS05012T1>

⁴<https://www.stereolabs.com/>

⁵<https://emlid.com/navio/>

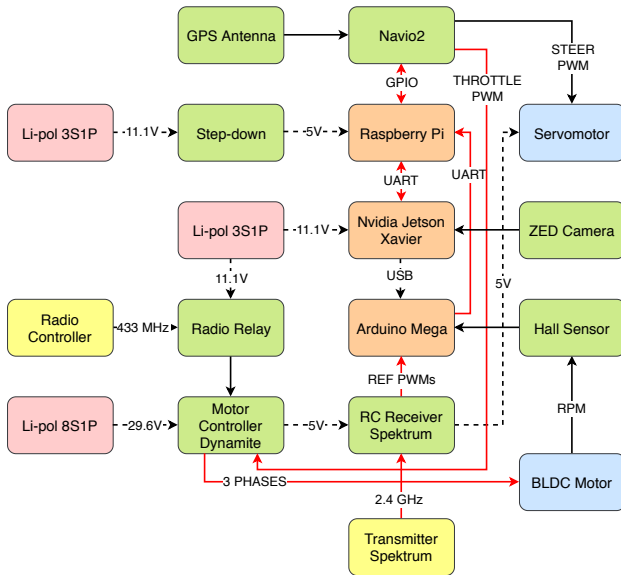


Fig. 9. Block diagram of the experimental platform.

gear. The system is equipped with RF remote emergency stop button.

The diagram of the system electronics is shown in Fig. 9. The core of the system is NVidia Jetson Xavier⁶, a powerful ARM computer with GPU (512-core Volta GPU with Tensor Cores, 16GB memory), running Ubuntu based operating system. There are two more computers: Raspberry Pi with the Navio-board handling the IMU+GPS and generating PWM signals for the throttle and steering, and Arduino processing the Hall sensor and collecting the remote signals.

Remote operations are either using manual signals from the RC transmitter, which are logged and forwarded to the motor controller, or run in assisted/autonomous mode, when the computer generates the signals for the motor controller. The system logs all sensors, all control signals including user inputs and stores camera images. All data are synchronized using GPS-based timestamps.

The RC car has no mechanical brakes and individual wheels cannot be controlled. We brake only via the traction motor and the torque propagates through the system of three differentials (front, rear, inter-axle) to the individual wheels; the middle differential was mechanically locked.

B. Visual Surface Recognition

We tested the semantic segmentation of the surface on independent test set of 100 real images with manually labeled ground-truth. The test images were captured by the platform camera in different locations than the training images. The CNN achieves average pixel-level accuracy 87%. Confusion among classes is depicted in Tab. II as the confusion matrix. The highest confusion occurs for the extra “Other” class, which has the highest intra-class variability.

To provide an intuition, we show segmentation maps in Fig. 1 and Fig. 4 of the experimental scene. The surface

⁶<https://developer.nvidia.com/embedded/jetson-agx-xavier-developer-kit>

		Predicted			
		Asphalt	Gravel	Grass	Other
Actual	Asphalt	86.8	3.1	9.7	0.4
	Gravel	0	99.4	0.6	0
	Grass	1.6	6.9	91.4	0.1
	Other	1.6	2.1	25.6	70.7

TABLE II
VISUAL SURFACE RECOGNITION – CONFUSION MATRIX.



Fig. 10. Subscale vehicle ride tests. Photos capture the platform after performing the collision avoidance maneuver on gravel. The operator initiates full braking immediately followed by the full right steer command.

consists of the the tarmac and a layer of gravel-like particles composed of wood and bark pieces, sand, fine gravel, and dried mud. The CNN was not trained on that particular surface, nevertheless it recognizes it mostly as the Gravel class. It is both visually similar as the gravel and it has similar friction properties. Minor errors are confusion with the grass (vegetation) or with the extra background class, which is in fact correct. The example demonstrates a good generalization to unseen classes. Note that especially in Fig. 4, we can see accurate segmentation of asphalt tracks appearing in the layer of the uneven gravel-like surface.

C. Drive tests results

We have realized ride experiments to evaluate improvements of the braking properties and namely maneuverability of the vehicle with the emulated visual feedback surface detection system. The vehicle performed intensive braking and simultaneous aggressive turn maneuvers on two surfaces with dramatically different friction properties. One was pure tarmac (Asphalt), and the second one was asphalt with dirt particles (Gravel). The vehicle speed right before the braking maneuver was 8.5 m/s. We evaluated the trajectories – namely the longitudinal travelled distance and the lateral achieved distance (the obstacle avoidance capability) – for three configurations:

- 1) no ABS assistance (ABS off),
- 2) ABS with correct parameters for the given surface
- 3) the “cross-test”, ABS with its parameters tuned for the wrong surface

Three trials were performed for each combination and the results are presented. To visualize the results, we show endpoints of the vehicle trajectory in polar plots, Fig. 11, where point (0,0) is the point where the vehicle started the maneuver. Axis 0° represents the heading vector before the maneuver started. The two plots are for two different surfaces, the Asphalt and the Gravel. Clearly,

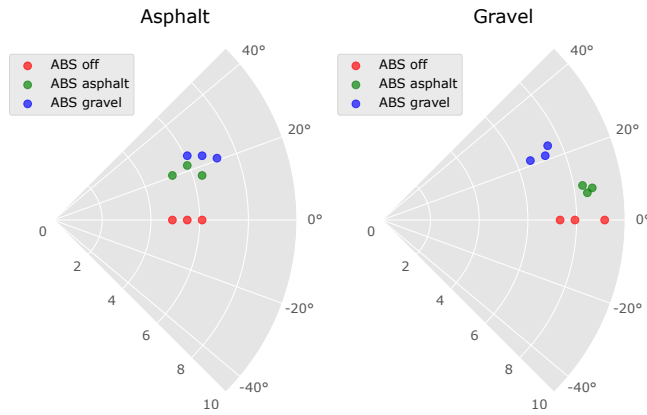


Fig. 11. Subscale vehicle ride tests. Polar graph visualization of endpoints of the trajectories after the collision avoidance maneuver.

- the braking performance is not significantly compromised if the ABS system (even with inadequate parameters) is applied
- the avoidance capability is improved significantly if the ABS system (even with inadequate parameters) is applied
- if the informed-version of the ABS system is applied, with parameters selected correctly for the given surface, the ABS performance is significantly enhanced - both in terms of the braking distance and avoidance capability.

It is seen that for both surfaces with ABS off, the vehicle does not turn at all despite full steering is set. This loss of directional control is a well known behaviour for vehicles without ABS. Moreover, the vehicle travels the longest distance until stopped on gravel. The ABS with parameters tuned for Asphalt naturally performs well on tarmac. The vehicle turns following the steering command, and it stops in a comparable distance as for the full uncontrolled braking. However on gravel (in case the surface misclassification problem appears), it performs much worse – the vehicle turns only slightly. The ABS with parameters set for Gravel excels on gravel – both in terms of obstacle avoidance capability and the stopping distance. In addition, it gives rise to acceptable performance on tarmac as well (slightly worse than a correct tarmac setting though).

The reported behaviour is confirmed by recordings from the on-board yaw-rate gyroscope. We present the yaw rate data from one gravel test in Fig. 12. In Fig. 10, we show the image of the vehicle reaching the end-point of the maneuver trajectory.

Please note that the supplementary video from the ride tests is provided with this submission.

VI. CONCLUSIONS

The concept of an anti-lock braking algorithm with camera-based augmentation was presented. The simulations based on a non-linear single track model indicate potentially significant reduction of braking distance compared to the current solutions. The total braking distance reduction of 14% is reported for a typical middle class sedan, under

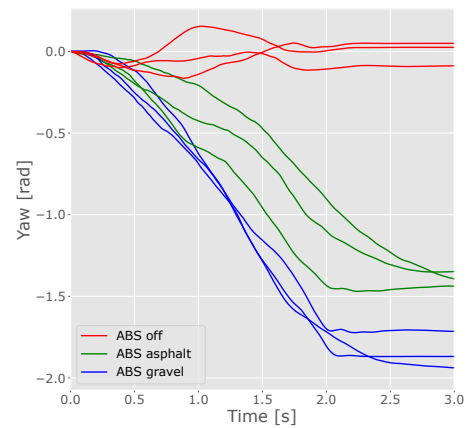


Fig. 12. Recordings of the yaw angle from the gyroscope during the brake-steer maneuver on gravel for all three braking algorithms. The ABS gravel follows the steering command the best.

specific complex road conditions, and for an emergency braking maneuver. Directional control consequences as well as performance of the surface recognition system and under real conditions and in real time were quantitatively assessed experimentally, using an instrumented subscale vehicle platform.

REFERENCES

- [1] H. Zhu, K.-V. Yuen, L. Mihaylova, and H. Leung, "Overview of environment perception for intelligent vehicles," *IEEE Trans. on Intelligent Transportation Systems*, vol. 18, no. 10, pp. 2584–2601, 2017.
- [2] R. B. GmbH, *Bosch Automotive Handbook, 10th Edition*. Wiley, 2018.
- [3] Loeber Motors blog, "What is Mercedes-Benz Magic Body Control?" 2015, <https://www.loebermotors.com/blog/mercedes-benz-magic-body-control/>.
- [4] J. Kim, J. Baek, H. Choi, and E. Kim, "Wet area and puddle detection for advanced driver assistance systems (ADAS) using a stereo camera," *International Journal of Control, Automation and Systems*, vol. 14, no. 1, pp. 263–271, 2016.
- [5] R. Omer and L. Fu, "An automatic image recognition system for winter road surface condition classification," in *Proc. of IEEE Conference on Intelligent Transportation Systems*, 2010, pp. 1375–1379.
- [6] P. Jonsson, "Remote sensor for winter road surface status detection," in *IEEE Sensors*, 2011.
- [7] R. Finkle, "Detection of ice layers on road surfaces using a polarimetric millimetre wave sensor at 76 GHz," *Electronics Letters*, vol. 33, no. 13, pp. 1153–1154, 1997.
- [8] R. Kees and J. Detlefsen, "Road surface classification by using a polarimetric coherent radar module at millimeter waves," in *Proc. of IEEE Telesystems Conference*, 1994, pp. 95–98.
- [9] V. Viikari, T. Varpula, and M. Kantanen, "Road-condition recognition using 24-GHz automotive radar," *IEEE Transactions on Intelligent Transportation Systems*, vol. 10, no. 4, pp. 639–648, 2009.
- [10] —, "Automotive radar technology for detecting road conditions. backscattering properties of dry, wet, and icy asphalt," in *Proc. of Radar Conference*, 2008, pp. 276–279.
- [11] R. B. D. Schramm, M. Hiller, *Vehicle Dynamics*. Springer, 2014.
- [12] H. Pacejka, *Tire and Vehicle Dynamics*. Elsevier, 2005.
- [13] J. Deng, W. Dong, R. Socher, L.-J. Li, K. Li, and L. Fei-Fei, "ImageNet: A Large-Scale Hierarchical Image Database," in *CVPR*, 2009.
- [14] O. Ronneberger, P. Fischer, and T. Brox, "U-Net: Convolutional networks for biomedical image segmentation," in *Medical Image Computing and Computer-Assisted Intervention*, 2015, pp. 234–241, <http://arxiv.org/abs/1505.04597>.